Target-oriented acquisition geometry design based on full-wavefield migration

Revelo-Obando, Billy; Blacquière, Gerrit

DOI
10.1190/GEO2023-0578.1

Publication date
2024

Document Version
Final published version

Published in
Geophysics

GEOPHYSICS, VOL. 89, NO. 3 (MAY-JUNE 2024); P. P21–P32, 19 FIGS.
10.1190/GEO2023-0578.1

Target-oriented acquisition geometry design based on full-wavefield migration

Billy Revelo-Obando[1] and Gerrit Blacquière[1]

ABSTRACT

The ultimate goal of survey design is to find the acquisition parameters that enable acquiring high-quality data suitable for optimal imaging, while fulfilling budget, health, safety, and environmental constraints. We develop a target-oriented acquisition design algorithm based on full-wavefield migration. The algorithm optimizes a receiver density function that indicates the number of receivers per unit area required for obtaining the best possible image quality. The method makes use of available seismic data to create a reference model that is included in our objective function. To make the design target oriented, the objective function is multiplied with a mask that gives more weight to the target areas of interest. The results of the 2D and 3D implementations indicate an optimized receiver density function with higher values at the zones where more data are needed for improving image quality. The corresponding receiver geometries have more receivers placed in these areas. We validate the results by computing the images of the target zone using uniform and optimized geometries. The use of the latter indicates an improvement in the image quality at the target zone. In addition, we compute the number of receivers required for achieving a certain signal-to-noise ratio after imaging based on the optimized receiver density function.

INTRODUCTION

Acquisition design for seismic surveys aims to optimize the acquisition parameters that enable adequate sampling of the seismic wavefield and noise. These parameters have to be adjusted according to the area under consideration, budget, expected signal properties, noise level, and health, safety, and environment constraints. Two of the acquisition parameters, namely the temporal and the spatial sampling interval, should ideally be chosen in such a way that signal and noise are recorded unaliased, i.e., these intervals satisfy the Nyquist criterion of more than two samples per smallest wavelength. For the temporal sampling interval, this is no problem, but for the spatial sampling interval, this is often not feasible due to the associated costs. The spatial sampling locations are determined by the positions of the seismic sources and the active receivers during each shot record, known as the active spread. This set of locations is known as the acquisition geometry. Knowing that the ideal geometry is not obtainable, it must be designed to achieve the following: adequate spatial sampling of the low-velocity noise, high trace multiplicity to achieve an acceptable signal-to-noise ratio (S/N), in particular at the subsurface target(s) of economic interest, and all these while fulfilling the economic constraints.

The spatial sampling requirements must also be selected according to the data processing algorithms that follow the data acquisition. In the preprocessing stage, for instance, noise-suppression algorithms are applied to improve the data quality. These algorithms may require a certain minimum spatial sampling to successfully remove the noise. In land acquisition, for example, the low-velocity noise such as ground roll may require a finer sampling than the signal of interest. For the purpose of imaging and velocity inversion, some algorithms may require a denser spatial sampling than others. Algorithms such as reverse time migration and Marchenko imaging, for instance, require densely sampled data (Wapenaar et al., 2014). When this is not possible, extra preprocessing steps such as data interpolation may be needed. In marine acquisition, algorithms such as full-wavefield migration (FWM) (Davydenko and Verschuur, 2017), which make use of multiple reflections for imaging, may require less dense spatial sampling and allow imaging below acquisition gaps, provided that the water bottom is sufficiently deep.

In a traditional acquisition geometry, sources and receivers are placed along straight lines. One of the most common types of land geometry is orthogonal geometry, in which the source and receiver lines are orthogonal to each other (Cordsen et al., 2000; Vermeer,

Manuscript received by the Editor 30 September 2023; revised manuscript received 18 December 2023; published ahead of production 17 January 2024; published online 26 February 2024.
[1]Delft University of Technology, Department of Geoscience and Engineering, Delft, The Netherlands. E-mail: billyrevelo@gmail.com (corresponding author); g.blacquiere-1@tudelft.nl.

DOI:10.1190/geo2023-0578.1

2012). The separation between these lines, their lengths, the spatial sampling along the lines, and the active spread determine the common-midpoint properties of the survey, such as offset distribution, azimuth, and fold (Vermeer, 2012). The fold and the S/N of the data dictate the resulting S/N of the final seismic product. Therefore, in areas in which a high level of incoherent noise is expected, the acquisition geometry should be adjusted to obtain a suitable S/N.

Ideally, in the noise-free case, the expected resolution of a seismic image could be computed from the acquisition aperture and the seismic bandwidth. However, in complex media, the wavefields illuminating the target zones and reflecting back to the acquisition surface are highly scattered, possibly resulting in a decreased illumination and detection of the target zone (Revelo-Obando and Blacquière, 2021). Therefore, in areas where prior information on the subsurface is available, the survey design can be adjusted to obtain better imaging.

One way to optimize the survey design is through the use of numerical modeling studies, in which a seismic experiment is simulated numerically to obtain the expected seismic image corresponding to a certain acquisition geometry. When the outcome of the experiment is not satisfactory, the acquisition geometry is manually adjusted (Theriot et al., 2014; Singh et al., 2016). This type of study does not provide a theoretical relation between the changes in the acquisition geometry and the resulting seismic image. Other types of model-based optimization studies use a seismic model to determine the location of seismic sources and receivers that allows maximizing the information content in full-waveform inversion (Maurer et al., 2010; Krampe et al., 2021; Winner et al., 2023).

In areas where seismic surveys have been carried out previously, legacy seismic data and corresponding seismic images are available. These can be used to optimize the design of a future survey. When the target area of economic interest has been identified, the acquisition geometry can be optimized to improve the illumination and detection properties at that target area. For instance, the focal beam analysis method (Volker et al., 2001; van Veldhuizen et al., 2008) is suitable for analyzing the illumination and resolution properties of a specific acquisition geometry at one particular subsurface target point. The method can also include additional illumination from multiple reflections (Kumar et al., 2016) or be used to automatically compute the acquisition geometry for optimum illumination at the target point (Wu et al., 2022). A similar illumination and resolution analysis can be performed through the use of point-spread functions, also called a resolution function (Berkhout, 1984; Beylkin, 1985; Lecomte and Gelius, 1998; Revelo-Obando and Blacquière, 2021).

The family of compressive sensing (CS) (Donoho, 2006) methods provides a framework for data acquisition and processing, which is based on irregular sampling (Herrmann, 2010). The sparse and irregularly sampled data can subsequently be recovered with transform-based recovery methods or matrix completion algorithms (Kumar et al., 2015). The irregular sampling for a seismic survey can be further improved by optimizing the spectral gap ratio of the survey design (Lopez et al., 2023).

In productive subsurface reservoirs, e.g., for carbon capture and storage, hydrocarbon production, and geothermal wells, the elastic properties of the reservoir change due to the injection and/or extraction of fluids or gases. Therefore, multiple surveys can be acquired at different time instances to monitor the changes in these properties. This type of acquisition is known as time-lapse or 4D acquisition. In the first 4D surveys, the acquisition and processing parameters are kept constant so that the changes in processed 3D volumes could be attributed to changes in the reservoir only (assuming that no changes in the overburden take place) (Greaves and Fulp, 1987). However, new techniques have been proposed to estimate the changes in the dynamic properties of the reservoir using data acquired with nonreplicated geometries (Oghenekohwo et al., 2017; Nakayama et al., 2019; Qu and Verschuur, 2020). In this case, at subsequent production stages, the survey design can be adjusted specifically to the target zone without replicating the baseline survey.

In this paper, we present an iterative algorithm based on our previous work (Revelo-Obando and Blacquière, 2023) for designing a target-oriented acquisition geometry. In this initial phase of our work, we assume the source geometry to be fixed and aim to optimize the receiver geometry, which we assume to be stationary. We parameterize the latter with a density function that is related to the number of receivers per unit area. This receiver density function is updated at each iteration using a gradient descent scheme. We propose an objective function that measures the difference between the image obtained with the current-iteration acquisition geometry and a reference image obtained with an ideal receiver distribution. To implement a target-oriented acquisition design, the objective function is computed using a spatially varying mask that puts more weight on the target zone and less weight on areas that are less important. The actual receiver positions are computed from the receiver density function with a weighted Voronoi stippling algorithm. The resulting receiver locations are irregularly distributed, such as in the case of CS. The receiver density is interpreted as a relative density, meaning that the actual number of receivers is chosen separately, e.g., depending on the expected noise level or the available equipment.

The paper is organized as follows. First, we lay out the framework of survey design and FWM. Subsequently, we define the parameterization and the target-oriented objective function. Next, we explain the iterative process that is the core of the optimization algorithm. Then, we show some case studies to demonstrate the performance of the algorithm. We finalize with some concluding remarks.

THEORY

Framework of the survey design

We describe 3D seismic data with the matrix notation introduced by Berkhout (1982). For a stationary acquisition geometry, one frequency component of a seismic data set can be formulated as

$$\mathbf{P}^{-}(z_d, z_s) = \mathbf{D}(z_d)\mathbf{X}^{-}(z_d, z_s)\mathbf{S}(z_s). \tag{1}$$

Matrix $\mathbf{P}^{-}$ is the upgoing acoustic pressure wavefield recorded at the acquisition level z_d and generated by the sources at the level z_s. Matrices $\mathbf{D}(z_d)$ and $\mathbf{S}(z_s)$ are the receiver and source matrices, respectively. They describe the acquisition geometry and contain the properties of the receivers and sources, such as sensitivity, directivity, and spectral properties. The superscripts $-$ and $+$ (which will appear subsequently) indicate wavefields in the upgoing and downgoing directions, respectively. Matrix $\mathbf{X}^{-}$ is the transfer operator of the subsurface, containing the propagation and reflection effects. It can be considered as the ideal data set, i.e., with fully sampled ideal point sources and receivers. If the sources and receivers are located at the surface z_0, i.e., $z_0 = z_s = z_d$, equation 1 becomes

DOI:10.1190/geo2023-0578.1

$$\mathbf{P}^{-}(z_0, z_0) = \mathbf{D}(z_0)\mathbf{X}^{-}(z_0, z_0)\mathbf{S}(z_0). \quad (2)$$

Assuming ideal fully sampled point sources, the matrix $\mathbf{S}(z_0)$ becomes the identity matrix $\mathbf{I}$. In this case, equation 2 becomes

$$\mathbf{P}^{-}(z_0, z_0) = \mathbf{D}(z_0)\mathbf{X}^{-}(z_0, z_0). \quad (3)$$

The modeling of the data set $\mathbf{X}^{-}(z_0, z_0)$ can be done with any modeling engine, e.g., with finite-difference modeling. We choose full-wavefield modeling (FWMod) (Berkhout, 2014). This is an iterative method that models the downgoing wavefield $\mathbf{X}_i^{+}(z_n, z_0)$ and the upgoing wavefield $\mathbf{X}_i^{-}(z_n, z_0)$ recursively in depth for N depth levels. At each iteration i, the downgoing wavefield is computed for $z_n = z_0, z_1, \ldots, z_N$ and, subsequently, the upgoing wavefield is computed for $z_n = z_N, z_{N-1}, \ldots, z_0$. Each iteration is called one round trip, as it starts with the downgoing wavefield at the surface z_0 and ends with the upgoing wavefield at the same level. At each round trip, one order of multiple reflections is added, starting with the primary reflections when $i = 0$ and adding the L-order multiple reflections for L iterations. It can be formulated as

$$\mathbf{X}_i^{+}(z_n, z_0) = \sum_{m=1}^{n-1} \mathbf{U}^{+}(z_n, z_m)\mathbf{R}^{\cap}(z_m)\mathbf{X}_{i-1}^{-}(z_m, z_0) + \mathbf{U}^{+}(z_n, z_0), \quad (4a)$$

$$\mathbf{X}_i^{-}(z_n, z_0) = \sum_{m=n+1}^{N} \mathbf{U}^{-}(z_n, z_m)\mathbf{R}^{\cup}(z_m)\mathbf{X}_i^{+}(z_m, z_0). \quad (4b)$$

This scheme is equivalent to a Bremmer series expansion (for details, see Davydenko, 2016). Matrices $\mathbf{R}^{\cap}(z_m)$ and $\mathbf{R}^{\cup}(z_m)$ are the up-down and down-up angle-dependent reflection operators at depth level z_m, respectively. Matrix $\mathbf{U}^{+}(z_n, z_m)$ includes all propagation and transmission effects of wavefields propagating in the downward direction from depth level z_m to depth level z_n, and so does operator $\mathbf{U}^{-}(z_n, z_m)$ for wavefields propagating in the upward direction. They are computed as follows:

$$\mathbf{U}^{+}(z_n, z_m) = \left[\prod_{k=n-1}^{m+1} \mathbf{W}^{+}(z_{k+1}, z_k)\mathbf{T}^{+}(z_k)\right]\mathbf{W}^{+}(z_{m+1}, z_m), \quad (5a)$$

$$\mathbf{U}^{-}(z_n, z_m) = \left[\prod_{k=n+1}^{m-1} \mathbf{W}^{-}(z_{k-1}, z_k)\mathbf{T}^{-}(z_k)\right]\mathbf{W}^{-}(z_{m-1}, z_m), \quad (5b)$$

where $\mathbf{W}^{+}(z_{k+1}, z_k)$ is the downward wavefield propagation operator from depth level z_k to depth level z_{k+1}, $\mathbf{W}^{-}(z_{k-1}, z_k)$ is the upward wavefield propagation operator from depth level z_k to depth level z_{k-1}, $\mathbf{T}^{+}(z_k)$ is the transmission operator of the downgoing wavefield crossing depth level z_k from above, and $\mathbf{T}^{-}(z_k)$ is the transmission operator of the upgoing wavefield crossing depth level z_k from below.

The use of this type of modeling allows us to specify the reflectivity and transmissivity independently from the propagation velocity. The output of this scheme, after L iterations, is the modeled perfectly sampled data $\mathbf{X}_L^{-}(z_0, z_0) = \mathbf{X}^{-}(z_0, z_0)$. The more realistic data set $\mathbf{P}_i(z_0, z_0)$ can be obtained via multiplication with $\mathbf{D}(z_0)$ (see equation 3) (still under the assumption of a perfect source distribution). As we discuss the acoustic case, the transmission operators can be described in terms of the reflectivity:

$$\mathbf{T}^{+}(z_k) = \mathbf{I} + \mathbf{R}^{\cup}(z_k), \quad (6a)$$

$$\mathbf{T}^{-}(z_k) = \mathbf{I} + \mathbf{R}^{\cap}(z_k). \quad (6b)$$

Reflectivity estimation with FWM

FWM is an iterative least-squares imaging algorithm that estimates a reflectivity model by minimizing the difference between the observed and synthetic data modeled through FWMod. During iteration i, the reflectivity is updated using a gradient descent scheme:

$$\mathbf{R}_{i+1}(z_n) = \mathbf{R}_i(z_n) + \alpha_i \delta\overline{\mathbf{R}}_i(z_n), \quad (7)$$

where $\delta\overline{\mathbf{R}}_i(z_n)$ is the update direction and α_i is the scaling parameter for the gradient descent scheme. The detailed derivation is discussed by Davydenko and Verschuur (2017).

METHOD

The method that we introduce in this paper is based on our previous work (Revelo-Obando and Blacquière, 2023). Our objective is to design the optimal receiver matrix $\mathbf{D}_i$ that leads to the best possible reflectivity estimate $\mathbf{R}_i$ given a fixed number of receivers n_d, which comes down to determining the optimum locations of these n_d receivers. This is done through an iterative process. At each iteration i, matrix $\mathbf{D}_i$ contains the position of the n_d receivers. The receiver locations are not completely arbitrary; they are located on a predefined grid.

Assuming ideal point receivers, i.e., with a flat unit sensitivity for each frequency component, matrix $\mathbf{D}_i(z_0)$ is a diagonal matrix whose elements are either one or zero, indicating the presence or absence of a receiver at a grid position, respectively. Therefore, updating the operator implies changing a zero into a one at certain locations while changing a one into a zero at an identical number of other locations. In this way, the total number of receivers does not change.

We assume that the fully sampled ideal data $\mathbf{X}^{-}(z_0, z_0)$ are available, i.e., modeled based on prior subsurface information. From these data, we create a reference image $\mathbf{R}$ through FWM using the velocity model from the same subsurface information. This image is considered the best possible reflectivity estimate (given the imaging method) as full receiver sampling is used. Therefore, at the end of each iteration, we compare the reflectivity estimate $\mathbf{R}_i$ with the reference image $\mathbf{R}$ through a target function that is introduced subsequently. We use a gradient descent scheme for minimizing this target function and updating the acquisition geometry. However, such a scheme requires a continuous real-valued function rather than the binary elements of matrix $\mathbf{D}_i$. Therefore, an intermediate parameterization is required. This is described in the next section.

Parameterization

We use a density function $\mathbf{\Phi}_i$ that indicates the relative density of receivers per unit area at the acquisition surface (Wu, 2020). This function is translated into an actual acquisition geometry through a transformation g as follows:

$$\mathbf{D}_i = g(\mathbf{\Phi}_i). \tag{8}$$

The transformation g is based on the weighted Voronoi stippling algorithm (Secord, 2002). First, the receivers are placed in a grid following a rejection sampling principle: the higher the value of the receiver density at a certain location, the higher the probability of a receiver being placed there. From these locations, a Voronoi diagram is computed and the receiver locations shifted toward the centroids of the Voronoi cells. The last two steps constitute Lloyd's algorithm (Lloyd, 1982). One of the advantages of using this parameterization is that the final receiver locations can be computed after the receiver density has been optimized. Therefore, the final choice of acquisition geometry could be made according to the available budget, equipment, or level of noise. The latter aspect will be discussed subsequently.

Figure 1 shows the transformation process. As an example, we create a density function that increases linearly from zero to one in the x-direction (Figure 1a). In the zone of smaller x coordinates, the density values are low. Consequently, fewer receivers per unit area are placed here (Figure 1b). The opposite occurs for the higher x coordinates: the density values are high, resulting in a large number of receivers per unit area.

Objective function

In our previous work, we introduce a least-squares objective function to measure the performance of an acquisition geometry. This objective function quantifies the absolute difference between the updated reflectivity image $\mathbf{R}_{i+1}(z_n)$, which is obtained with the current acquisition geometry $\mathbf{D}_i$ and the reference image $\mathbf{R}(z_n)$. The objective function is defined as

$$J_{R,i} = \sum_n \|\Delta\mathbf{R}_i(z_n)\|_F^2, \tag{9a}$$

$$\Delta\mathbf{R}_i(z_n) = \mathbf{R}(z_n) - \mathbf{R}_{i+1}(z_n). \tag{9b}$$

The residual $\Delta\mathbf{R}_i$ is the difference between the reference image and the new estimate. The initial reflectivity image $\mathbf{R}_1(z_n)$ is obtained after one FWM iteration using an initial receiver geometry $\mathbf{D}_i$ for $i = 0$ and with n_d receivers. We now introduce a modification of the objective function that gives more weight to one or more target zones. In this way, the focus is to obtain an acquisition geometry that enables better imaging of these target zones. For this purpose, we apply a mask $\mathbf{\Psi}(z_n)$ that scales the residual image:

$$J_{T,i} = \sum_n \|\mathbf{\Psi}(z_n)\Delta\mathbf{R}_i(z_n)\|_F^2, \tag{10}$$

where $J_{T,i}$ is the new target-oriented objective function. Matrix $\mathbf{\Psi}(z_n)$ is a spatially varying weighting function whose elements range between zero and one. Target zones are given higher values than zones of less importance. In the case that a uniform image quality is desired, matrix $\mathbf{\Psi}$ must be filled with equal numbers.

Gradient descent scheme

The receiver density function is updated through an iterative gradient descent scheme:

$$\mathbf{\Phi}_{i+1} = \mathbf{\Phi}_i + \beta_i \delta\mathbf{\Phi}_i, \tag{11}$$

where $\mathbf{\Phi}_i$ is the current-iteration receiver density, $\delta\mathbf{\Phi}_i$ is the update direction, β_i is the step length, and $\mathbf{\Phi}_{i+1}$ is the updated next-iteration receiver density.

Update direction and step length

The update direction for the receiver density is related to the gradient of the objective function $J_{T,i}$ (equation 10) with respect to receiver density $\mathbf{\Phi}$. Therefore, the derivative to be computed is

$$\frac{\partial J_{T,i}}{\partial \mathbf{\Phi}} = \frac{\partial}{\partial \mathbf{\Phi}}\left[\sum_n \|\mathbf{\Psi}(z_n)\Delta\mathbf{R}_i(z_n)\|_F^2\right]. \tag{12}$$

As demonstrated in Appendix A, this derivative can be expressed as

$$\frac{\partial J_{T,i}}{\partial \mathbf{\Phi}} = -2\alpha_i \sum_n \sum_\omega \Delta\mathbf{P}_r(\mathbf{\Psi}(z_n)\Delta\mathbf{R}_i(z_n))[\Delta\mathbf{X}_i^-(z_0, z_0)]^H, \tag{13}$$

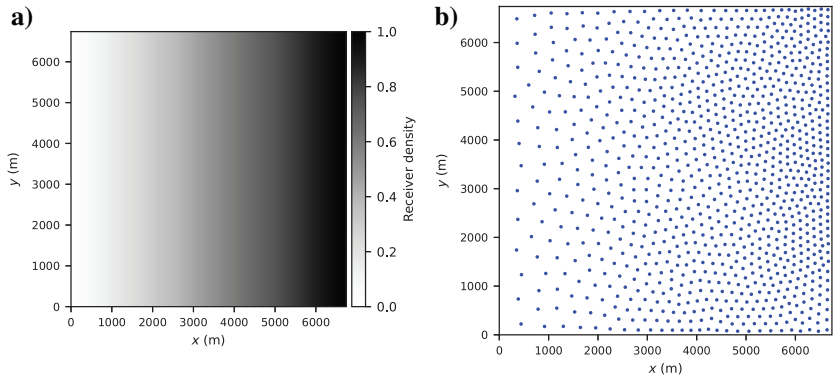

Figure 1. (a) Relative receiver density and (b) receiver geometry created through the transformation g for $n_d = 1000$.

where $\Delta\mathbf{X}_i^-$ is the data residual, i.e., the difference between the modeled and reference data. The term $\Delta\mathbf{P}_r$ is a seismic wavefield modeled from the weighted residual image $\mathbf{\Psi}(z_n)\Delta\mathbf{R}_i$. Equation 13 contains the correlation between this wavefield and the data residual $\Delta\mathbf{X}_i^-$. Therefore, it can be interpreted as a mapping from the model domain, specifically the scaled residual image, to the data domain, indicating the sampling locations where more data are needed to improve the imaging of the target zone.

The update direction is given by the negative conjugate of equation 13:

$$\delta\mathbf{\Phi}_i = -\frac{\partial J_{T,i}^*}{\partial\mathbf{\Phi}}, \tag{14}$$

and the step length (Appendix B) is given by

$$\beta_i = \frac{(\delta\Phi_i)^H\delta\Phi_i}{\mathrm{diag}\left\{-2\alpha_i\sum_n\sum_\omega\Delta\mathbf{P}_r(\mathbf{\Psi}(z_n)\mathbf{R}_\phi(z_n))[\Delta\mathbf{X}_i^-(z_0,z_0)]^H\right\}^H\delta\Phi_i}, \tag{15}$$

where $\delta\Phi_i$ is a vector obtained from $\delta\Phi_i = \mathrm{diag}\{\delta\mathbf{\Phi}_i\}$. Matrix $\mathbf{R}_\phi(z_n)$ is an image associated with the receiver density update direction in equation 14 and $\Delta\mathbf{P}_r(\mathbf{\Psi}(z_n)\mathbf{R}_\phi(z_n))$ is the corresponding wavefield perturbation.

Before updating the receiver density function, we apply a spatial filter to the update direction in equation 14 to smooth the gradient and account for possible unstable behavior caused by sparse 3D acquisition geometries. Subsequently, the receiver density function can be updated using equation 11. The resulting updated density $\mathbf{\Phi}_{i+1}$ is transformed into the new acquisition geometry $\mathbf{D}_{i+1}$ through the transformation g.

Algorithm

As a start, the reference reflectivity model $\mathbf{R}(z_n)$ and a propagation velocity model, i.e., operator $\mathbf{W}$, are obtained from legacy seismic data and/or other available information, e.g., from a neighboring area. From this reference model, perfect seismic data $\mathbf{X}^-(z_0,z_0)$, i.e., fully sampled, are modeled. These data are used as the observed data during FWM. At each iteration of the algorithm, the current receiver geometry is applied to the fully sampled data set, leading to the practical data $\mathbf{P}_i^-(z_0,z_0) = \mathbf{D}_i(z_0)\mathbf{X}_i^-(z_0,z_0)$. With these data, one iteration of FWM is performed, updating the reflectivity estimate from $\mathbf{R}_i(z_n)$ to $\mathbf{R}_{i+1}(z_n)$. Subsequently, the objective function $J_{T,i}$ is evaluated. If the updated reflectivity does not satisfy a predefined quality criterion ε, the acquisition geometry is updated. The quality of this geometry is evaluated through a new FWM iteration and repetition of the aforementioned steps until the quality criterion is satisfied.

The iterative process to optimize the receiver geometry is summarized in Figure 2. In the next section, it will be discussed whether it may be necessary to change the number of receivers n_d and restart this process.

Modifying the number of receivers

The output of our algorithm is the optimized receiver density $\mathbf{\Phi}$. This function is related to the number of receivers per unit area. This means that multiple acquisition geometries with different numbers of receivers can be generated. In practice, this number of receivers can be chosen based on constraints such as the available hardware, or a minimum target S/N, that depends on the field noise level. In the case of incoherent noise, the S/N is expected to increase with a higher number of receivers.

To determine the number of required receivers that are necessary to achieve a certain S/N, we model the seismic data $\mathbf{P}^- = \mathbf{D}\mathbf{X}^-$ with n_d receivers and add realistic seismic noise. Using these data, $\mathbf{\Phi}$ is computed with our algorithm. Next, we generate an acquisition geometry $\mathbf{D}_\kappa$ with κn_d receivers, where κ is a factor that can be larger or smaller than one, corresponding to more or fewer receivers, and apply it to obtain seismic data $\mathbf{P}_\kappa^- = \mathbf{D}_\kappa\mathbf{X}^-$. Then, through FWM, we obtain the corresponding image $\mathbf{R}_\kappa(z_n)$ and compute the corresponding S/N. Depending on the outcome, we either increase or decrease κ and repeat the procedure until the S/N criterion is met. We use white noise to demonstrate how this principle works.

RESULTS

2D implementation

First, we tested our algorithm with a 2D implementation. We used a slice of the SEG salt model (Figure 3). We then created synthetic data via FWMod and did imaging via FWM using full

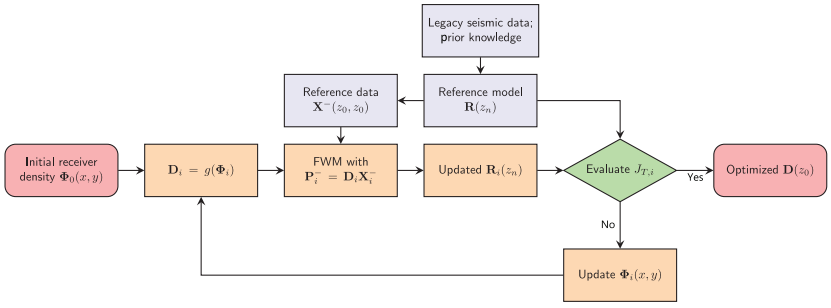

Figure 2. Algorithm for target-oriented acquisition design. The blocks in blue are the steps required to obtain the reference model and data. The blocks in orange are part of the iterative loop to update the acquisition geometry.

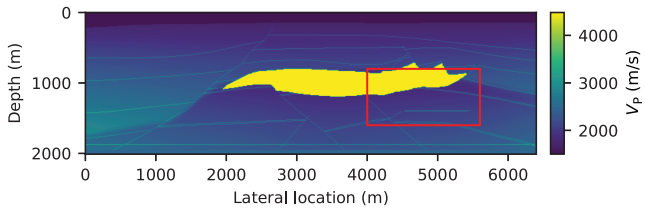

Figure 3. The 2D section of the SEG salt model. The red rectangle delimits the target zone.

receiver sampling to create the reference reflectivity model. The sources were uniformly distributed every 400 m.

We aim to optimize a sparse acquisition geometry with $n_d = 20$ receivers. These are initially located uniformly at the acquisition surface $z_0 = 0$m (Figure 4). In the first experiment, we use a uniform mask $\mathbf{\Phi}$, i.e., all the elements of the matrix have a value of one. Therefore, no extra weight is given to any zone and the design is not target oriented. We call the resulting geometry optimized design (Figure 5).

The results in Figure 5 show that the optimized receiver density is rather homogeneous. The separation between the receivers in the corresponding receiver geometry is almost constant. Subsequently, we use an acquisition mask $\mathbf{\Phi}$ that gives more weight to the zone contained within the red box in Figure 3. We assume that the area under the salt dome in this section is of interest and we aim to obtain a better image of this target zone. We call the resulting geometry target-oriented design (Figure 6). It shows higher density values on the right side of the model, roughly above the target zone, than in the rest of the model. The corresponding receiver geometry has more receivers located in this area than on the left side.

To evaluate the effect of the optimized geometries on the image quality, we compare the images obtained with the optimized design (Figure 5) and the target-oriented design (Figure 6). The results are shown in Figure 7b and 7c, respectively. The reference image, i.e., obtained with dense spatial sampling, is shown in Figure 7a. The image obtained with the target-oriented geometry (Figure 7c) shows better continuity in the region delineating the salt dome than the image obtained from the optimized design (Figure 7b). The underlying reflector is also better defined. The S/N improvement in the image quality of the target zone is 0.47 dB with respect to the optimized geometry and 0.58 dB with respect to the uniform geometry.

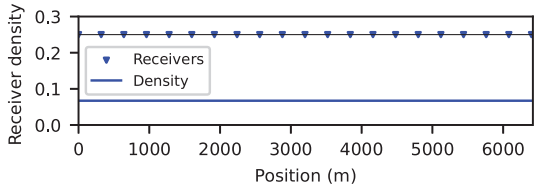

Figure 4. Starting geometry for the model in Figure 3.

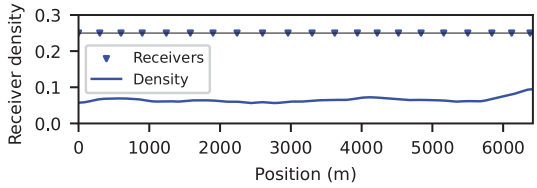

Figure 5. Optimized geometry for the model in Figure 3.

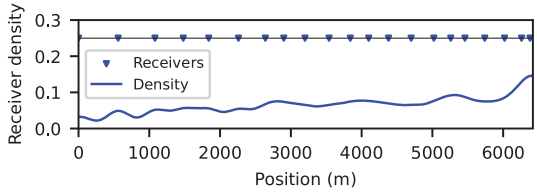

Figure 6. Target-oriented geometry.

Computing the number of receivers

To illustrate the procedure for computing the number of receivers described in the previous section, we use the model in Figure 8. This model contains horizontal layers with a high-velocity perturbation embedded in the first layer.

We use our optimization algorithm to compute the optimized receiver density (Figure 9). The resulting function is higher in the region above the high-velocity perturbation than at the edges, where the model is less complex. This indicates that more receivers are needed in this area to improve image quality. The corresponding receiver geometry for the case of $n_d = 24$ receivers is also plotted.

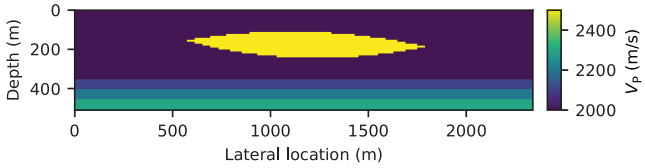

Figure 8. Model with high-velocity perturbation.

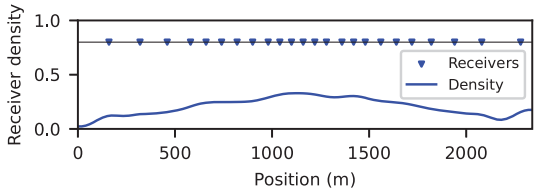

Figure 9. Optimized receiver density and corresponding receiver geometry for $n_d = 24$.

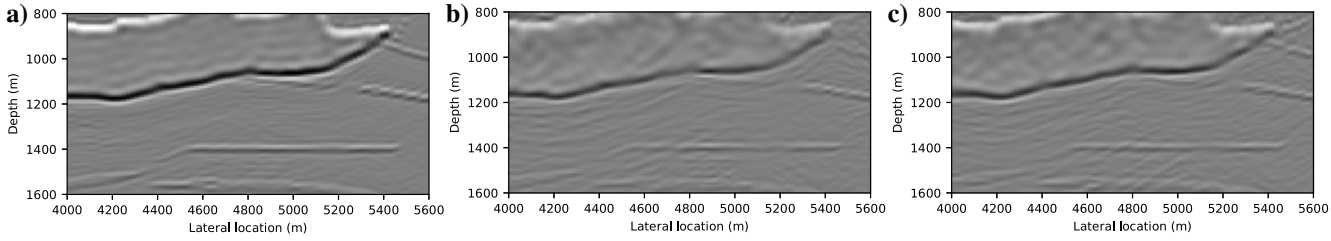

Figure 7. Comparison of the images of the target zone: (a) reference image obtained with dense spatial sampling, (b) image obtained with the optimized design, and (c) image obtained with the target-oriented design.

From the optimized receiver density, we generate several receiver geometries with different numbers of receivers n_d. We assume that it is desired to obtain an image with an S/N of 15 dB. We add white noise to the data to simulate the acquisition noise. Subsequently, we compute the images associated with the generated receiver geometries. Each one has an associated S/N after imaging. We plot the resulting S/N versus n_d in Figure 10.

Figure 10 shows that there are two points for $n_d = 24$ receivers. The point with a lower S/N corresponds to a uniform acquisition geometry. The point with a higher S/N corresponds to the image obtained when using the optimized receiver geometry in Figure 9. The rest of the points show how the S/N is increasing for an increasing number of receivers. The S/N obtained when doubling the number of receivers from 24 to 48 is approximately 6 dB higher, as expected. The red horizontal line in Figure 10 shows that the desired S/N of 15 dB is obtained when using $n_d = 44$ receivers.

3D results

We test the 3D implementation of the algorithm with the model, as shown in Figure 11. It contains a high-velocity intrusion that runs along the y-direction.

The (fixed) source geometry consists of sources located every 200 m in the x- and y-directions. The initial receiver geometry and density are uniform and these are shown in Figure 12.

In the first experiment, we run our algorithm to obtain the optimized geometry. Therefore, no extra weight is given to any area. The results are shown in Figure 13.

The optimized receiver density in Figure 13b shows that the density is relatively somewhat higher in the zone above the high-velocity intrusion that runs along the y-direction. It is also higher in the lower y values. This could be due to the presence of the thin (orange) layer at the bottom that only appears for this range of y values. Otherwise, the receiver distribution is rather uniform. Subsequently, we compute the target-oriented geometry using a mask that gives more weight to a zone approximately in the middle of the model: with x ranging from 1000 to 1500 m, y ranging from 700 to 900 m, and z ranging from 440 to 600 m. The target-oriented design is shown in Figure 14.

The target-oriented receiver density is shown in Figure 14b. As expected, it is higher in the center, i.e., roughly above the target zone, than the original receiver density in Figure 13b. This indicates that more receivers are needed in this area to obtain a better image quality of this zone.

Finally, we test our 3D implementation with the SEG salt model (Figure 15). We create a reference model by using a densely sampled receiver geometry, i.e., receivers every 20 m in the x- and y-directions. We consider a uniform sparse source geometry with $n_s = 36$ sources. The initial receiver geometry is a uniform grid with receivers every 400 m in the x- and y-directions, for a total of $n_d = 17 \times 17 = 289$ receivers (Figure 16a). The corresponding receiver density function is uniform (Figure 16b).

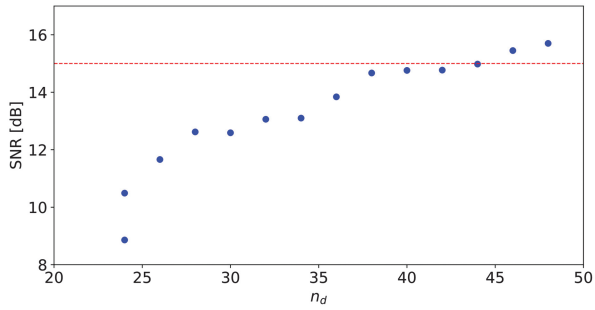

Figure 10. Imaging S/N versus the number of receivers. The dashed horizontal line indicates that $n_d = 44$ receivers are necessary to achieve an S/N of 15 dB.

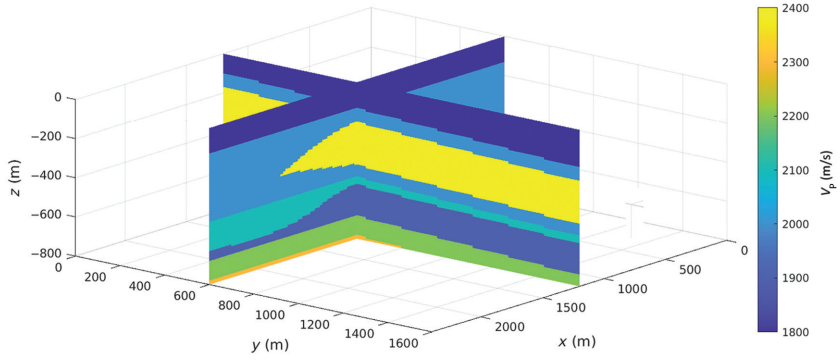

Figure 11. The 3D model with high-velocity perturbation along the y-axis.

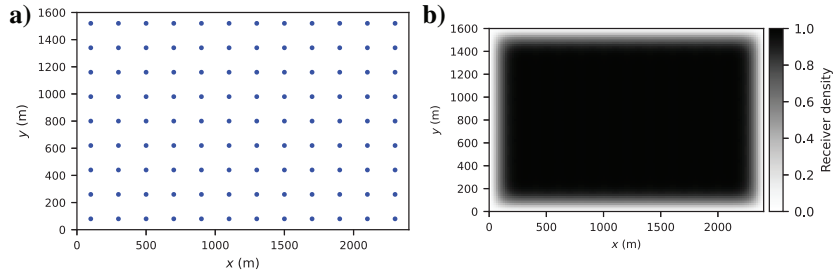

Figure 12. (a) Initial uniform receiver geometry and (b) receiver density for the model in Figure 11.

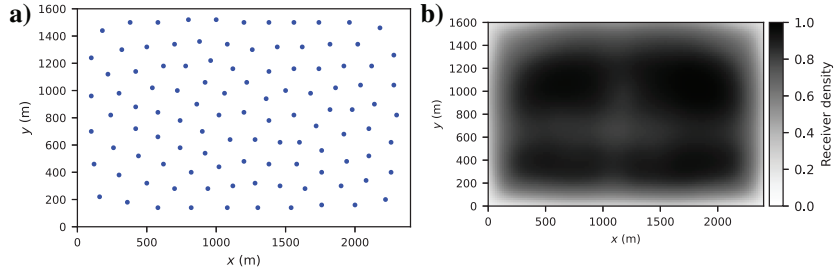

Figure 13. (a) Optimized receiver geometry obtained from the (b) optimized receiver density for the model in Figure 11.

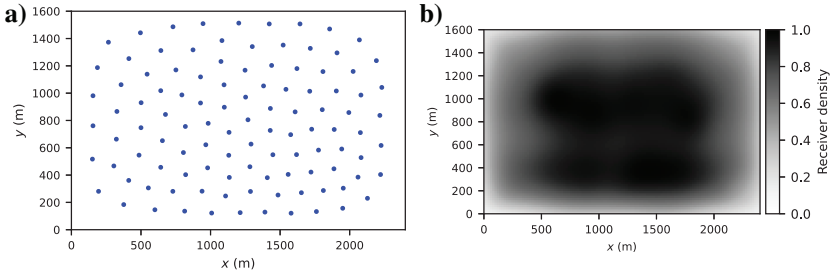

Figure 14. (a) Target-oriented receiver geometry obtained from the (b) target-oriented receiver density for the model in Figure 11.

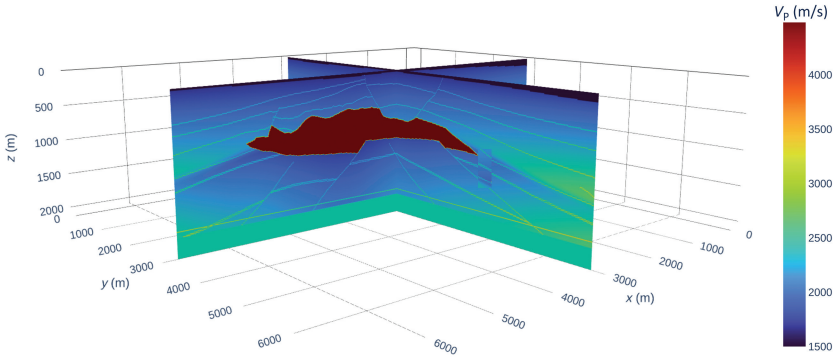

Figure 15. SEG salt model.

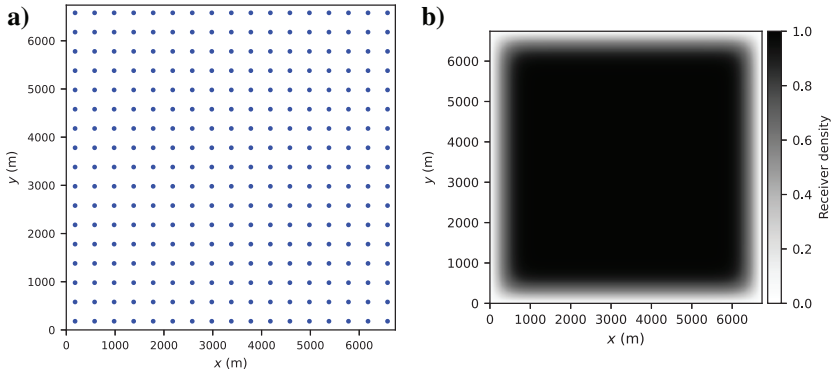

Figure 16. (a) Initial uniform receiver geometry and (b) receiver density for the model in Figure 15.

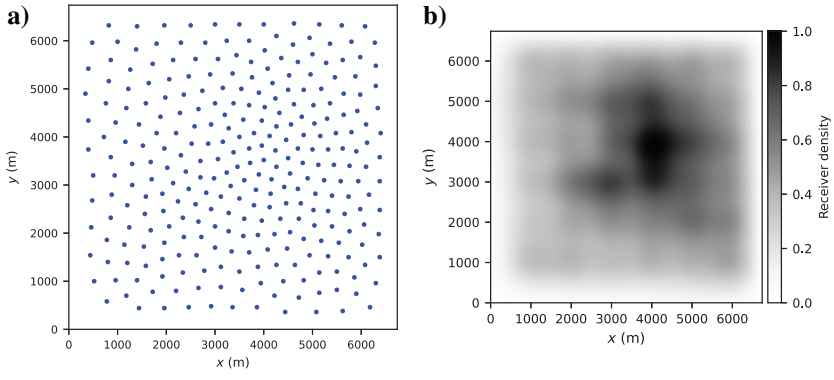

Figure 17. (a) Optimized receiver geometry obtained from the (b) optimized receiver density for the model in Figure 15.

Using the reference model and the initial geometry shown in Figure 16, we compute the optimized acquisition design (Figure 17). The optimized receiver density (Figure 17b) is higher at the center of the acquisition surface, above the top of the salt dome, than at the edges, resulting in an acquisition geometry with more receivers placed in this area (Figure 17a). This could be due to the presence of the high-velocity salt dome which is located roughly at the center of the model. Subsequently, we compute the target-oriented design, with a mask that gives more weight to the region with x ranging from 2000 to 3000 m, y ranging from 2000 to 3000 m, and z ranging from 1000 to 1500 m. This region corresponds to an area of possible interest beneath the salt dome. The resulting target-oriented design is shown in Figure 18.

The target-oriented geometry in Figure 18 clearly shows a higher density close to the area above the designated target zone (x = 2000–3000 m and y = 2000–3000 m) than the optimized geometry in Figure 17. To validate these results, we compare the images of the target zone obtained via FWM using the uniform geometry (Figure 16a), the optimized geometry (Figure 17a), and the target-oriented geometry (Figure 18a). The best possible scenario, i.e., the image obtained with full receiver sampling, is included as a reference (Figure 19a). The results are plotted in Figure 19.

The image in the target zone obtained with the target-oriented geometry (Figure 19d) shows a better delineation of the salt region than the image obtained with the optimized geometry (Figure 19c). As expected, the improvement is larger when comparing the former with the image obtained with the uniform geometry (Figure 19b). The target-oriented geometry offers an improvement of 1.74 dB in the image quality with respect to the uniform geometry, whereas the optimized design offers an improvement of 1.15 dB with respect to the uniform geometry. This upgrade in the image quality shows that uplift is possible even when using a sparse geometry: we used $n_d = 289$ receivers in the target-oriented design, whereas the reference image was obtained with approximately 400 times more receivers.

DISCUSSION

The optimized acquisition geometries obtained in our examples consist of irregularly located receivers. To implement such an acquisition geometry in practice, nodal acquisition systems would be required either in marine or land scenarios. In this way, the receivers can be individually located without the constraints of wired connections. The design of the final acquisition geometry must also take into account the possible processing limitations that could arise from

sparse spatial sampling. Because the data acquired with such geometry will be irregularly sampled, when using a low number of receivers, acquisition gaps could be present in the geometry design. Therefore, the subsequent processing must be able to deal with these data, i.e., the combination of the chosen imaging algorithm and its use of multiple reflections in the area under consideration should enable optimal imaging in the areas where there are gaps.

The optimized density function is independent of the noise and the acquisition geometry generated from it, and so it could be adjusted to the conditions in the field. In principle, any type of realistic noise can be taken into account at the moment of choosing the final acquisition geometry. In the case of incoherent noise, the S/N will increase by 3 dB when the number of receivers is doubled. However, when the noise is coherent, this relationship may not hold and another approach may be needed, such as manually imposing constraints in the density function or adding extra weight in the target mask that accounts for noisy areas.

This paper deals with the optimization of the receiver geometry assuming a constant source geometry. Because image quality is directly influenced by the illumination provided by the sources, in future work, optimizing their geometry could complement the benefits offered by the optimized receiver geometry. In practice, this could be achieved by adding relatively more shooting or vibration locations in the areas indicated by the algorithm. Blended acquisition could also be taken into account, potentially increasing the spatial sampling offered by the source geometry and/or further reducing costs.

The algorithm for acquisition geometry optimization uses FWM as the imaging engine. From the implementation point of view, this saves computational costs because the wavefields $\mathbf{X}^{+}$ and $\mathbf{X}^{-}$ are computed only once for receiver density and reflectivity updates. However, in principle, any imaging engine that uses multiples for imaging could be incorporated into the algorithm.

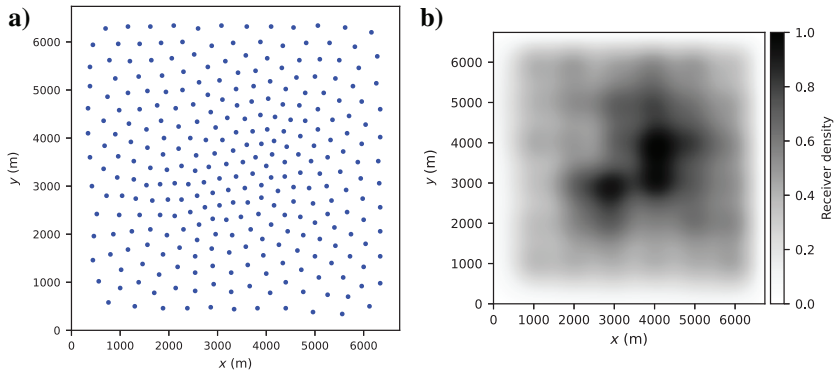

Figure 18. (a) Target-oriented receiver geometry obtained from the (b) target-oriented receiver density for the model in Figure 15.

CONCLUSION

We propose a new algorithm that enables the design of target-oriented acquisition geometries. Our 3D algorithm makes use of multiple reflections for imaging via FWM and enables the design of sparse acquisition geometries that improve the image quality at the target zone. The imaging results obtained when using the target-oriented design show that the image quality at the target zone

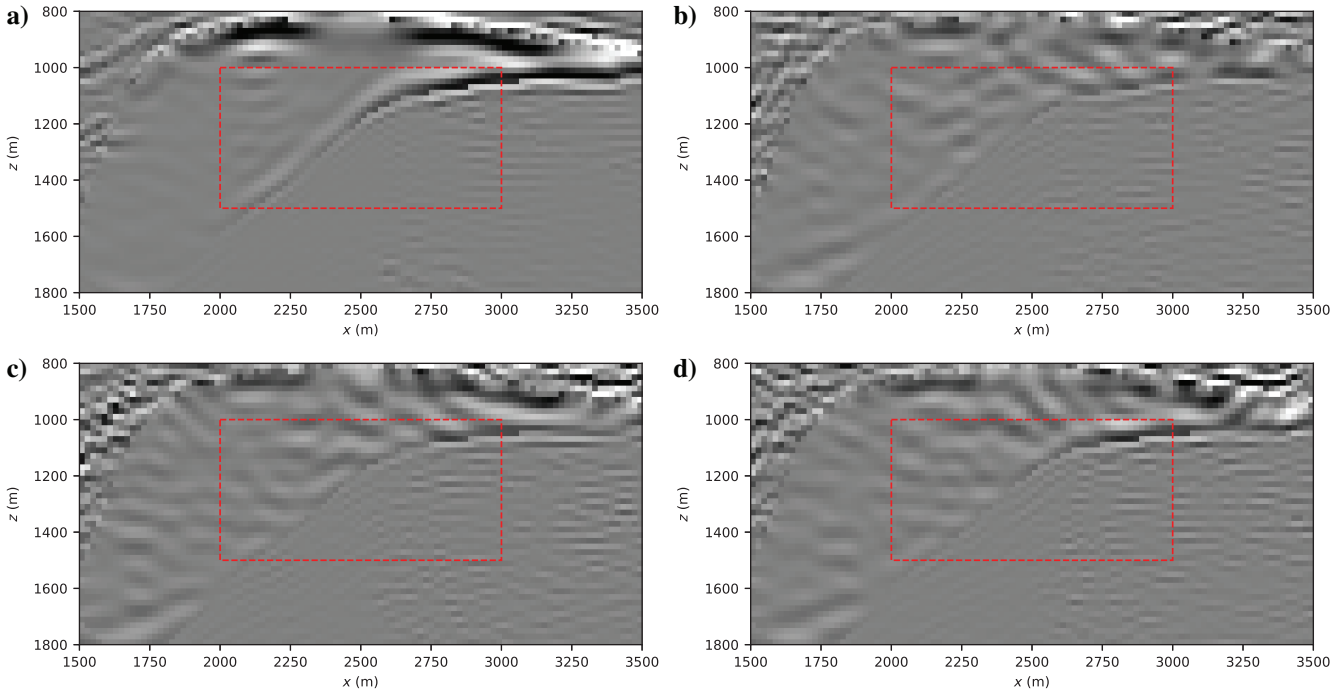

Figure 19. Comparison of images obtained using different acquisition geometries. Slice at y = 2400 m. The target zone is enclosed by the dashed red line: (a) Imaging using dense spatial sampling, (b) imaging with the uniform geometry in Figure 16, (c) imaging with the optimized geometry in Figure 17, and (d) imaging with the target-oriented geometry in Figure 18.

is better than when using a uniform geometry. In addition, we illustrate how the number of receivers required to obtain a certain S/N after imaging can be computed from the optimized receiver density. In practice, based on the expected noise level during acquisition, the available hardware, and financial constraints, an optimized receiver geometry that allows a target S/N could be computed. In our examples, we only consider the case of white noise. However, in reality, acquisition noise is much more complex, and other types of noise could be modeled to better resemble the conditions in the field.

ACKNOWLEDGMENTS

The authors thank the sponsors of the Delphi Consortium for their support.

DATA AND MATERIALS AVAILABILITY

Data associated with this research are confidential and cannot be released.

APPENDIX A

DERIVATION OF THE UPDATE DIRECTION

We repeat equation 12 as being the derivative of target function $J_{T,i}$ with respect to the receiver density $\mathbf{\Phi}$:

$$\frac{\partial J_{T,i}}{\partial \mathbf{\Phi}} = \frac{\partial}{\partial \mathbf{\Phi}}\left[\sum_n \|\mathbf{\Psi}(z_n)\Delta\mathbf{R}_i(z_n)\|_F^2\right]. \tag{A-1}$$

Using the definition of the Frobenius norm, we rewrite this expression as

$$\frac{\partial J_{T,i}}{\partial \mathbf{\Phi}} = \frac{\partial}{\partial \mathbf{\Phi}}\left[\sum_n \mathrm{Tr}[(\mathbf{\Psi}(z_n)\Delta\mathbf{R}_i(z_n))(\mathbf{\Psi}(z_n)\Delta\mathbf{R}_i(z_n))^H]\right]. \tag{A-2}$$

To find the derivative in equation A-2, it is necessary to express $\Delta\mathbf{R}_i(z_n)$ in terms of $\mathbf{\Phi}$. Using equation 7, the term $\Delta\mathbf{R}(z_n)$ can be written as

$$\Delta\mathbf{R}_i(z_n) = \mathbf{R}(z_n) - \mathbf{R}_i(z_n) - \alpha_i\delta\overline{\mathbf{R}}_i(z_n). \tag{A-3}$$

From equation 9b, it follows that $\Delta\mathbf{R}_{i-1}(z_n) = \mathbf{R}(z_n) - \mathbf{R}_i(z_n)$. By substituting this in equation A-3, we obtain

$$\Delta\mathbf{R}_i(z_n) = \Delta\mathbf{R}_{i-1}(z_n) - \alpha_i\delta\overline{\mathbf{R}}_i(z_n). \tag{A-4}$$

The reflectivity update direction $\delta\overline{\mathbf{R}}_i(z_n)$ (Davydenko and Verschuur, 2017) can be expressed as

$$\delta\overline{\mathbf{R}}_i(z_n) = \delta\overline{\mathbf{R}}_i^{\cup}(z_n) - \delta\overline{\mathbf{R}}_i^{\cap}(z_n), \tag{A-5}$$

where the overbar indicates the angle-independent reflectivity approximation. The terms $\delta\overline{\mathbf{R}}_i^{\cup}(z_n)$ and $\delta\overline{\mathbf{R}}_i^{\cap}(z_n)$ are the down-up and up-down reflectivity update directions, respectively. They are defined as

$$\delta\overline{\mathbf{R}}_i^{\cup}(z_n) = \mathrm{diag}\left\{\sum_\omega [\mathbf{U}_i^-(z_0,z_n)]^H\Delta\mathbf{P}_i(z_0,z_0)[\mathbf{X}_i^+(z_n,z_0)]^H\right\}, \tag{A-6a}$$

$$\delta\overline{\mathbf{R}}_i^{\cap}(z_n) = \mathrm{diag}\left\{\sum_\omega [\mathbf{U}_i^{\cup}(z_0,z_n)]^H\Delta\mathbf{P}_i(z_0,z_0)[\mathbf{X}_{i-1}^-(z_n,z_0)]^H\right\}, \tag{A-6b}$$

where $\mathrm{diag}\{\mathbf{M}\}$ clears all off-diagonal elements of matrix $\mathbf{M}$. For notational brevity, we will omit this part of the notation in the remainder of this paper. The term $\Delta\mathbf{P}_i(z_0,z_0)$ is the data residual at iteration i obtained with the current acquisition geometry $\mathbf{D}_i(z_0)$. It is defined as follows:

$$\Delta\mathbf{P}_i(z_0,z_0) = \mathbf{D}_i(z_0)\Delta\mathbf{X}_i^-(z_0,z_0), \tag{A-7a}$$

with

$$\Delta\mathbf{X}_i^-(z_0,z_0) = \mathbf{X}^-(z_0,z_0) - \mathbf{X}_i^-(z_0,z_0). \tag{A-7b}$$

By substituting equation A-5 in equation A-4, we obtain

$$\Delta\mathbf{R}_i(z_n) = \Delta\mathbf{R}_{i-1}(z_n) - \alpha_i[\delta\overline{\mathbf{R}}_i^{\cup}(z_n) - \delta\overline{\mathbf{R}}_i^{\cap}(z_n)]. \tag{A-8}$$

Subsequently, we replace equations A-6a and A-6b in equation A-8:

$$\begin{aligned}\Delta\mathbf{R}_i(z_n) = \Delta\mathbf{R}_{i-1}(z_n) - \alpha_i\sum_\omega &[[\mathbf{U}_i^-(z_0,z_n)]^H\Delta\mathbf{P}_i(z_0,z_0)[\mathbf{X}_i^+(z_n,z_0)]^H \\ &- [\mathbf{U}_i^{\cup}(z_0,z_n)]^H\Delta\mathbf{P}_i(z_0,z_0)[\mathbf{X}_{i-1}^-(z_n,z_0)]^H].\end{aligned} \tag{A-9}$$

Then, we replace equation A-7a in equation A-9:

$$\begin{aligned}\Delta\mathbf{R}_i(z_n) = \Delta\mathbf{R}_{i-1}(z_n) - \alpha_i\sum_\omega &[[\mathbf{U}_i^-(z_0,z_n)]^H\mathbf{D}_i(z_0)\Delta\mathbf{X}_i^-(z_0,z_0)[\mathbf{X}_i^+(z_n,z_0)]^H \\ &- [\mathbf{U}_i^{\cup}(z_0,z_n)]^H\mathbf{D}_i(z_0)\Delta\mathbf{X}_i^-(z_0,z_0)[\mathbf{X}_{i-1}^-(z_n,z_0)]^H].\end{aligned} \tag{A-10}$$

To move along the direction of the steepest descent, finite real-valued updates are needed for the acquisition geometry. Therefore, instead of using the receiver matrix $\mathbf{D}_i(z_0)$, we use the receiver density matrix $\mathbf{\Phi}_i(z_0)$ in equation A-7a, which then becomes

$$\Delta\mathbf{P}_i(z_0,z_0) = \mathbf{\Phi}_i(z_0)\Delta\mathbf{X}_i^-(z_0,z_0). \tag{A-11}$$

Subsequently, we substitute equation A-11 in equation A-10 and obtain

$$\begin{aligned}\Delta\mathbf{R}_i(z_n) = \Delta\mathbf{R}_{i-1}(z_n) - \alpha_i\sum_\omega &[[\mathbf{U}_i^-(z_0,z_n)]^H\mathbf{\Phi}_i(z_0)\Delta\mathbf{X}_i^-(z_0,z_0)[\mathbf{X}_i^+(z_n,z_0)]^H \\ &- [\mathbf{U}_i^{\cup}(z_0,z_n)]^H\mathbf{\Phi}_i(z_0)\Delta\mathbf{X}_i^-(z_0,z_0)[\mathbf{X}_{i-1}^-(z_n,z_0)]^H].\end{aligned} \tag{A-12}$$

Therefore, we can write the term $\mathbf{\Psi}(z_n)\Delta\mathbf{R}_i(z_n)$ as

$$\mathbf{\Psi}(z_n)\Delta\mathbf{R}_i(z_n) = \mathbf{A}_1\mathbf{Y}\mathbf{B}_1 - \mathbf{A}_2\mathbf{Y}\mathbf{B}_2 + \mathbf{C}, \tag{A-13}$$

where

$$\mathbf{A}_1 = -\alpha_i\mathbf{\Psi}(z_n)\sum_\omega [\mathbf{U}_i^-(z_0,z_n)]^H, \tag{A-14a}$$

$$\mathbf{A}_2 = -\alpha_i \boldsymbol{\Psi}(z_n) \sum_{\omega} [\mathbf{U}_i^{\cup}(z_0, z_n)]^H, \tag{A-14b}$$

$$\mathbf{B}_1 = \Delta\mathbf{X}_i^{-}(z_0, z_0)[\mathbf{X}_i^{+}(z_n, z_0)]^H, \tag{A-14c}$$

$$\mathbf{B}_2 = \Delta\mathbf{X}_i^{-}(z_0, z_0)[\mathbf{X}_{i-1}^{-}(z_n, z_0)]^H, \tag{A-14d}$$

$$\mathbf{C} = \boldsymbol{\Psi}(z_n)\Delta\mathbf{R}_{i-1}(z_n), \tag{A-14e}$$

$$\mathbf{Y} = \boldsymbol{\Phi}(z_0). \tag{A-14f}$$

Using this notation, we can write the derivative in equation A-2 as

$$\frac{\partial J_{T,i}}{\partial \boldsymbol{\Phi}} = \sum_n \frac{\partial}{\partial \mathbf{Y}} \mathrm{Tr}[(\mathbf{A}_1\mathbf{Y}\mathbf{B}_1 - \mathbf{A}_2\mathbf{Y}\mathbf{B}_2 + \mathbf{C})(\mathbf{A}_1\mathbf{Y}\mathbf{B}_1 - \mathbf{A}_2\mathbf{Y}\mathbf{B}_2 + \mathbf{C})^H]. \tag{A-15}$$

We expand the right side of equation A-15 and obtain

$$\begin{aligned}\frac{\partial J_{T,i}}{\partial \boldsymbol{\Phi}} = \frac{\partial}{\partial \mathbf{Y}} \mathrm{Tr}(&\mathbf{A}_1\mathbf{Y}\mathbf{B}_1\mathbf{B}_1^H\mathbf{Y}^H\mathbf{A}_1^H - \mathbf{A}_1\mathbf{Y}\mathbf{B}_1\mathbf{B}_2^H\mathbf{Y}^H\mathbf{A}_2^H + \mathbf{A}_1\mathbf{Y}\mathbf{B}_1\mathbf{C}^H \\ &- \mathbf{A}_2\mathbf{Y}\mathbf{B}_2\mathbf{B}_1^H\mathbf{Y}^H\mathbf{A}_1^H + \mathbf{A}_2\mathbf{Y}\mathbf{B}_2\mathbf{B}_2^H\mathbf{Y}^H\mathbf{A}_2^H - \mathbf{A}_2\mathbf{Y}\mathbf{B}_2\mathbf{C}^H \\ &+ \mathbf{C}\mathbf{B}_1^H\mathbf{Y}^H\mathbf{A}_1^H - \mathbf{C}\mathbf{B}_2^H\mathbf{Y}^H\mathbf{A}_2^H + \mathbf{C}\mathbf{C}^H).\end{aligned} \tag{A-16}$$

To find the derivatives in equation A-16, we make use of the next two identities (Petersen and Pedersen, 2012):

$$\frac{\partial}{\partial \mathbf{Y}} \mathrm{Tr}(\mathbf{A}\mathbf{Y}\mathbf{B}\mathbf{Y}^H\mathbf{C}) = \mathbf{A}^H\mathbf{C}^H\mathbf{Y}\mathbf{B}^H + \mathbf{C}\mathbf{A}\mathbf{Y}\mathbf{B}, \tag{A-17}$$

$$\frac{\partial}{\partial \mathbf{Y}} \mathrm{Tr}(\mathbf{A}\mathbf{Y}^H\mathbf{B}) = \mathbf{B}\mathbf{A}. \tag{A-18}$$

By applying equations A-17 and A-18 to equation A-16, we obtain the expression

$$\begin{aligned}\frac{\partial J_{T,i}}{\partial \boldsymbol{\Phi}} = &\mathbf{A}_1^H\mathbf{A}_1\mathbf{Y}\mathbf{B}_1\mathbf{B}_1^H + \mathbf{A}_1^H\mathbf{A}_1\mathbf{Y}\mathbf{B}_1\mathbf{B}_1^H - \mathbf{A}_1^H\mathbf{A}_2\mathbf{Y}\mathbf{B}_2\mathbf{B}_1^H - \mathbf{A}_2^H\mathbf{A}_1\mathbf{Y}\mathbf{B}_1\mathbf{B}_2^H \\ &+ \mathbf{A}_1^H\mathbf{C}\mathbf{B}_1^H - \mathbf{A}_2^H\mathbf{A}_1\mathbf{Y}\mathbf{B}_1\mathbf{B}_2^H - \mathbf{A}_1^H\mathbf{A}_2\mathbf{Y}\mathbf{B}_2\mathbf{B}_1^H + \mathbf{A}_2^H\mathbf{A}_2\mathbf{Y}\mathbf{B}_2\mathbf{B}_2^H \\ &+ \mathbf{A}_2^H\mathbf{A}_2\mathbf{Y}\mathbf{B}_2\mathbf{B}_2^H - \mathbf{A}_2^H\mathbf{C}\mathbf{B}_2^H + \mathbf{A}_1^H\mathbf{C}\mathbf{B}_1^H - \mathbf{A}_2^H\mathbf{C}\mathbf{B}_2^H,\end{aligned} \tag{A-19}$$

which can be further reduced to

$$\begin{aligned}\frac{\partial J_{T,i}}{\partial \boldsymbol{\Phi}} = &2\mathbf{A}_1^H(\mathbf{A}_1\mathbf{Y}\mathbf{B}_1 - \mathbf{A}_2\mathbf{Y}\mathbf{B}_2 + \mathbf{C})\mathbf{B}_1^H \\ &- 2\mathbf{A}_2^H(\mathbf{A}_1\mathbf{Y}\mathbf{B}_1 - \mathbf{A}_2\mathbf{Y}\mathbf{B}_2 + \mathbf{C})\mathbf{B}_2^H.\end{aligned} \tag{A-20}$$

Finally, by substituting equations A-14a–A-14f in equation A-20, we obtain

$$\begin{aligned}\frac{\partial J_{T,i}}{\partial \boldsymbol{\Phi}} = -2\alpha_i \sum_n \sum_{\omega} &[\mathbf{U}_i^{-}(z_0, z_n)\boldsymbol{\Psi}(z_n)\Delta\mathbf{R}_i(z_n)\mathbf{X}_i^{+}(z_n, z_0) \\ &- \mathbf{U}_i^{\cup}(z_0, z_n)\boldsymbol{\Psi}(z_n)\Delta\mathbf{R}_i(z_n)\mathbf{X}_{i-1}^{-}(z_n, z_0)][\Delta\mathbf{X}_i^{-}(z_0, z_0)]^H.\end{aligned} \tag{A-21}$$

The first term between braces in equation A-21 is a modeled wavefield based on the weighted residual reflectivity image $\boldsymbol{\Psi}(z_n)\Delta\mathbf{R}_i(z_n)$. We define it as

$$\begin{aligned}\Delta\mathbf{P}_r(\Psi(z_n)\Delta\mathbf{R}_i(z_n)) = &\mathbf{U}_i^{-}(z_0, z_n)\boldsymbol{\Psi}(z_n)\Delta\mathbf{R}_i(z_n)\mathbf{X}_i^{+}(z_n, z_0) \\ &- \mathbf{U}_i^{\cup}(z_0, z_n)\boldsymbol{\Psi}(z_n)\Delta\mathbf{R}_i(z_n)\mathbf{X}_{i-1}^{-}(z_n, z_0).\end{aligned} \tag{A-22}$$

Therefore, we replace equation A-22 in equation A-21 and obtain

$$\frac{\partial J_{T,i}}{\partial \boldsymbol{\Phi}} = -2\alpha_i \sum_n \sum_{\omega} \Delta\mathbf{P}_r(\boldsymbol{\Psi}(z_n)\Delta\mathbf{R}_i(z_n))[\Delta\mathbf{X}_i^{-}(z_0, z_0)]^H. \tag{A-23}$$

Equation A-23 contains the correlation between the data residual $\Delta\mathbf{X}_i^{-}$ and the wavefield $\Delta\mathbf{P}_r$ modeled from the residual reflectivity image $\boldsymbol{\Psi}(z_n)\Delta\mathbf{R}_i$. Therefore, it can be interpreted as a mapping from the model update to the data space, at the sampling locations where more data are needed. Finally, the update direction is given by

$$\delta\boldsymbol{\Phi}_i = -\frac{\partial J_{T,i}^*}{\partial \boldsymbol{\Phi}}. \tag{A-24}$$

APPENDIX B

DERIVATION OF THE SCALING PARAMETER

In the gradient descent scheme, the optimal scaling parameter is found when the update direction at iteration $i+1$ is orthogonal to the direction at iteration i (Shewchuk, 1994). Therefore, the following condition must hold:

$$[\delta\boldsymbol{\Phi}_{i+1}]^H\delta\boldsymbol{\Phi}_i = 0. \tag{B-1}$$

To find the update direction $\delta\boldsymbol{\Phi}_{i+1}$, we use equation A-23 and assume that the term $\boldsymbol{\Phi}$, which is implicitly contained, can be linearized:

$$\delta\boldsymbol{\Phi}_{i+1} = -2\alpha_i \sum_n \sum_{\omega} [\Delta\mathbf{P}_r(\boldsymbol{\Psi}(z_n)\Delta\mathbf{R}_i(z_n))]_{\boldsymbol{\Phi}}[\Delta\mathbf{X}_i^{-}(z_0, z_0)]^H. \tag{B-2}$$

The subscript $\boldsymbol{\Phi}$ in this and subsequent equations refers to the variables computed for finding the optimal scaling parameter, which means in the direction of $\delta\boldsymbol{\Phi}_{i+1}$. The wavefield $[\Delta\mathbf{P}_r(\boldsymbol{\Psi}(z_n)\Delta\mathbf{R}_i(z_n))]_{\boldsymbol{\Phi}}$ is therefore

$$\begin{aligned}[\Delta\mathbf{P}_r(\boldsymbol{\Psi}(z_n)\Delta\mathbf{R}_i(z_n))]_{\boldsymbol{\Phi}} = &\mathbf{U}_i^{-}(z_0, z_n)[\boldsymbol{\Psi}(z_n)\Delta\mathbf{R}_i(z_n)]_{\boldsymbol{\Phi}}\mathbf{X}_i^{+}(z_n, z_0) \\ &+ \mathbf{U}_i^{\cup}(z_0, z_n)[\boldsymbol{\Psi}(z_n)\Delta\mathbf{R}_i(z_n)]_{\boldsymbol{\Phi}}\mathbf{X}_{i-1}^{-}(z_n, z_0),\end{aligned} \tag{B-3}$$

where $[\Delta\mathbf{R}_i(z_n)]_{\boldsymbol{\Phi}}$ is an image obtained from

$$[\Delta\mathbf{R}_i(z_n)]_{\mathbf{\Phi}} = \mathbf{\Psi}(z_n)\Delta\mathbf{R}_{i-1}(z_n) - \alpha_i\mathbf{\Psi}(z_n)\sum_{\omega}\{[\mathbf{U}_i^{-}(z_0,z_n)]^H\mathbf{\Phi}_{i+1}\Delta\mathbf{X}_i^{-}(z_0,z_0)[\mathbf{X}_i^{+}(z_n,z_0)]^H + [\mathbf{U}_i^{\cup}(z_0,z_n)]^H\mathbf{\Phi}_{i+1}\Delta\mathbf{X}_i^{-}(z_0,z_0)[\mathbf{X}_{i-1}^{-}(z_n,z_0)]^H\}. \quad \text{(B-4)}$$

In equation B-4, the receiver density $\mathbf{\Phi}_{i+1}$ is used instead of $\mathbf{\Phi}_i$. Therefore, we may substitute equation 11 in equation B-4:

$$[\Delta\mathbf{R}_i(z_n)]_{\mathbf{\Phi}} = \mathbf{\Psi}(z_n)\Delta\mathbf{R}_{i-1}(z_n) - \alpha_i\mathbf{\Psi}(z_n)\sum_{\omega}\{[\mathbf{U}_i^{-}(z_0,z_n)]^H(\mathbf{\Phi}_i+\beta_i\delta\mathbf{\Phi}_i)\Delta\mathbf{X}_i^{-}(z_0,z_0)[\mathbf{X}_i^{+}(z_n,z_0)]^H + [\mathbf{U}_i^{\cup}(z_0,z_n)]^H(\mathbf{\Phi}_i+\beta_i\delta\mathbf{\Phi}_i)\Delta\mathbf{X}_i^{-}(z_0,z_0)[\mathbf{X}_{i-1}^{-}(z_n,z_0)]^H\}. \quad \text{(B-5)}$$

By substituting equation B-5 in equation B-3, and substituting the result in equation B-2, we obtain

$$\delta\mathbf{\Phi}_{i+1} = \delta\mathbf{\Phi}_i - 2\alpha_i\beta_i\sum_n\sum_{\omega}\Delta\mathbf{P}_r(\mathbf{\Psi}(z_n)\mathbf{R}_{\phi}(z_n))[\Delta\mathbf{X}_i^{-}(z_0,z_0)]^H, \quad \text{(B-6)}$$

where matrix $\mathbf{R}_{\phi}(z_n)$ is an image obtained from:

$$\mathbf{R}_{\phi}(z_n) = -2\alpha_i\sum_{\omega}\{[\mathbf{U}_i^{-}(z_0,z_n)]^H\delta\mathbf{\Phi}_i\Delta\mathbf{X}_i^{-}(z_0,z_0)[\mathbf{X}_i^{+}(z_n,z_0)]^H. + [\mathbf{U}_i^{\cup}(z_0,z_n)]^H\delta\mathbf{\Phi}_i\Delta\mathbf{X}_i^{-}(z_0,z_0)[\mathbf{X}_{i-1}^{-}(z_n,z_0)]^H\}. \quad \text{(B-7)}$$

Finally, by substituting equation B-6 in equation B-1, we obtain the optimal scaling parameter:

$$\beta_i = \frac{(\delta\Phi_i)^H\delta\Phi_i}{\text{diag}\left\{-2\alpha_i\sum_n\sum_{\omega}\Delta\mathbf{P}_r(\mathbf{\Psi}(z_n)\mathbf{R}_{\phi}(z_n))[\Delta\mathbf{X}_i^{-}(z_0,z_0)]^H\right\}^H\delta\Phi_i}. \quad \text{(B-8)}$$

In equation B-8, the denominator is computed following these steps:

1) Compute the reflectivity image $\mathbf{R}_{\phi}(z_n)$.
2) From this image, model seismic data $\Delta\mathbf{P}_r(\mathbf{\Psi}(z_n)\mathbf{R}_{\phi}(z_n))$.
3) Correlate these data with the data residual $\Delta\mathbf{X}_i^{-}(z_0,z_0)$.
4) Correlate this result with the current update direction $\delta\Phi_i$.

REFERENCES

Berkhout, A., 2014, Review paper: An outlook on the future of seismic imaging, Part II: Full-wavefield migration: Geophysical Prospecting, **62**, 931–949, doi: 10.1111/1365-2478.12154.

Berkhout, A. J., 1982, Seismic migration: Imaging of acoustic energy by wave field extrapolation. A. Theoretical aspects: Elsevier.

Berkhout, A. J., 1984, Seismic resolution: A quantitative analysis of resolving power of acoustical echo techniques: Geophysical Press, Handbook of Geophysical Exploration 12.

Beylkin, G., 1985, Imaging of discontinuities in the inverse scattering problem by inversion of a causal generalized Radon transform: Journal of Mathematical Physics, **26**, 99–108, doi: 10.1063/1.526755.

Cordsen, A., M. Galbraith, and J. Peirce, 2000, Planning land 3-D seismic surveys: SEG.

Davydenko, M., 2016, Full wavefield migration: Seismic imaging using multiple scattering effects: Ph.D. thesis, Delft University of Technology.

Davydenko, M., and D. Verschuur, 2017, Full-wavefield migration: Using surface and internal multiples in imaging: Geophysical Prospecting, **65**, 7–21, doi: 10.1111/1365-2478.12360.

Donoho, D., 2006, Compressed sensing: IEEE Transactions on Information Theory, **52**, 1289–1306, doi: 10.1109/TIT.2006.871582.

Greaves, R. J., and T. J. Fulp, 1987, Three-dimensional seismic monitoring of an enhanced oil recovery process: Geophysics, **52**, 1175–1187, doi: 10.1190/1.1442381.

Herrmann, F. J., 2010, Randomized sampling and sparsity: Getting more information from fewer samples: Geophysics, **75**, no. 6, WB173–WB187, doi: 10.1190/1.3506147.

Krampe, V., P. Edme, and H. Maurer, 2021, Optimized experimental design for seismic full waveform inversion: A computationally efficient method including a flexible implementation of acquisition costs: Geophysical Prospecting, **69**, 152–166, doi: 10.1111/1365-2478.13040.

Kumar, A., G. Blacquière, and E. Verschuur, 2016, Extending illumination using all multiples: Application to 3D acquisition geometry analysis: Geophysical Prospecting, **64**, 622–641, doi: 10.1111/1365-2478.12326.

Kumar, R., C. Da Silva, O. Akalin, A. Y. Aravkin, H. Mansour, B. Recht, and F. J. Herrmann, 2015, Efficient matrix completion for seismic data reconstruction: Geophysics, **80**, no. 5, V97–V114, doi: 10.1190/geo2014-0369.1.

Lecomte, I., and L.-J. Gelius, 1998, Have a look at the resolution of prestack depth migration for any model, survey and wavefields: 68th Annual International Meeting, SEG, Expanded Abstracts, 1112–1115, doi: 10.1190/1.1820082.

Lloyd, S., 1982, Least squares quantization in PCM: IEEE Transactions on Information Theory, **28**, 129–137, doi: 10.1109/TIT.1982.1056489.

Lopez, O., R. Kumar, N. Moldoveanu, and F. J. Herrmann, 2023, Spectral gap-based seismic survey design: IEEE Transactions on Geoscience and Remote Sensing, **61**, 1–9, doi: 10.1109/TGRS.2023.3237464.

Maurer, H., A. Curtis, and D. E. Boerner, 2010, Recent advances in optimized geophysical survey design: Geophysics, **75**, no. 5, 75A177–75A194, doi: 10.1190/1.3484194.

Nakayama, S., G. Blacquière, and T. Ishiyama, 2019, Acquisition design for direct reflectivity and velocity estimation from blended and irregularly sampled data: Geophysical Prospecting, **67**, 2127–2146, doi: 10.1111/1365-2478.12841.

Oghenekohwo, F., H. Wason, E. Esser, and F. J. Herrmann, 2017, Low-cost time-lapse seismic with distributed compressive sensing — Part 1: Exploiting common information among the vintages: Geophysics, **82**, no. 3, P1–P13, doi: 10.1190/geo2016-0076.1.

Petersen, K. B., and M. S. Pedersen, 2012, The matrix cookbook: Technical University of Denmark.

Qu, S., and D. J. Verschuur, 2020, Simultaneous joint migration inversion for high resolution imaging/inversion of time-lapse seismic datasets: Geophysical Prospecting, **68**, 1167–1188, doi: 10.1111/1365-2478.12918.

Revelo-Obando, B., and G. Blacquière, 2021, Acquisition geometry analysis with point-spread functions: Geophysical Prospecting, **69**, 1606–1624, doi: 10.1111/1365-2478.13128.

Revelo-Obando, B., and G. Blacquière, 2023, Seismic acquisition design based on full-wavefield migration: Geophysics, **88**, no. 3, P37–P49, doi: 10.1190/geo2022-0313.1.

Secord, A., 2002, Weighted Voronoi stippling: Proceedings of the 2nd International Symposium on Non-Photorealistic Animation and Rendering, Association for Computing Machinery, 37–43.

Shewchuk, J. R., 1994, An introduction to the conjugate gradient method without the agonizing pain: Technical Report, Carnegie Mellon University.

Singh, V., A. Venkataraman, R. Ho, E. Neumann, and B. Laugier, 2016, Ocean-bottom node acquisition optimization: 86th Annual International Meeting, SEG, Expanded Abstracts, 193–197, doi: 10.1190/segam2016-13958824.1.

Theriot, C., M. McDonald, M. R. Kamarudin, and P. Yu, 2014, Survey design for optimized ocean bottom node acquisition: 84th Annual International Meeting, SEG, Expanded Abstracts, 213–217, doi: 10.1190/segam2014-1438.1.

van Veldhuizen, E. J., G. Blacquière, and A. J. Berkhout, 2008, Acquisition geometry analysis in complex 3D media: Geophysics, **73**, no. 5, Q43–Q58, doi: 10.1190/1.2972029.

Vermeer, G. J. O., 2012, 3D seismic survey design, 2nd ed.: SEG, Geophysical References Series 2.

Volker, A. W. F., G. Blacquière, A. J. Berkhout, and L. Ongkiehong, 2001, Comprehensive assessment of seismic acquisition geometries by focal beams — Part II: Practical aspects and examples: Geophysics, **66**, 918–931, doi: 10.1190/1.1444982.

Wapenaar, K., J. Thorbecke, J. van der Neut, F. Broggini, E. Slob, and R. Snieder, 2014, Marchenko imaging: Geophysics, **79**, no. 3, WA39–WA57, doi: 10.1190/geo2013-0302.1.

Winner, V., P. Edme, and H. Maurer, 2023, Model-based optimization of source locations for 3D acoustic seismic full-waveform inversion: Geophysical Prospecting, **71**, 3–16, doi: 10.1111/1365-2478.13264.

Wu, S., 2020, Optimising marine seismic acquisition: Source encoding in blended acquisition and target-oriented acquisition geometry optimisation: Ph.D. thesis, Delft University of Technology.

Wu, S., D. J. Verschuur, and G. Blacquière, 2022, Automated seismic acquisition geometry design for optimized illumination at the target: A linearized approach: IEEE Transactions on Geoscience and Remote Sensing, **60**, 1–13, doi: 10.1109/TGRS.2021.3131365.

Biographies and photographs of the authors are not available.